Materials Science & Engineering A 798 (2020) 140247

Contents lists available at ScienceDirect

Materials Science & Engineering A

journal homepage: http://www.elsevier.com/locate/msea

Investigation of the influences of ternary Mg addition on the solidification microstructure and mechanical properties of as-cast Al–10Si alloys

Qiang Li [a,b], Feng Qiu [a,b,*], Bai-Xin Dong [a,b], Hong-Yu Yang [a,c,**], Shi-Li Shu [d], Min Zha [a,b], Qi-Chuan Jiang [a,b]

[a] State Key Laboratory of Automotive Simulation and Control, Jilin University, PR China
[b] Key Laboratory of Automobile Materials, Ministry of Education and Department of Materials Science and Engineering, Jilin University, Renmin Street NO. 5988, Changchun, Jilin Province, 130025, PR China
[c] School of Materials Science and Engineering, Jiangsu University of Science and Technology, Zhenjiang, 212003, China
[d] School of Mechanical and Aerospace Engineering, Jilin University, Renmin Street NO. 5988, Changchun, Jilin Province, 130025, PR China

ARTICLE INFO

Keywords:
Hypoeutectic Al–10Si alloys
Ternary Mg solute
Thermal analysis
Solidification behavior
Multi-refinement
Mechanical properties

ABSTRACT

A hypoeutectic Al–10Si-2.0 Mg ternary alloy with high strength and high ductility was developed for as-cast service conditions. The effects of eutectic-forming element Mg on the primary α-Al dendrites, eutectic Si structure, Mg_2Si intermetallic compound, mechanical properties and fracture behavior were systematically investigated via multiscale characterization methods. Interestingly, the results demonstrated that with the increasing Mg content, the secondary dendrite arm spacings of the primary α-Al dendrites were significantly reduced, and the grain size was refined, while the flaky eutectic Si structure was fully modified into a coral-like morphology. Additionally, the size of the Mg_2Si intermetallic phase sharply decreased, and it was distributed much more uniformly in the interdendritic/intergranular eutectic regions. In contrast with the binary Al–10Si alloy, the yield strength, the ultimate tensile strength and the fracture strain were substantially enhanced to 159.4 MPa, 275.3 MPa and 14.1%, respectively, which correspond to improvements of 131.0%, 70.4% and 27.0%, respectively. The underlying mechanisms that were responsible for the evolution of the microstructure and mechanical properties are explicitly discussed.

1. Introduction

Hypoeutectic Al–10Si-based foundry alloys have received extensive attention due to their superior fluidity, high strength/density ratio and outstanding corrosion resistance, especially in automotive and aerospace applications, in which large and complex three-dimensional geometric structural components are ever-increasingly demanded [1–3]. All these attractive characteristics are attributable to the narrow solidification range and the excellent combination of the soft aluminum matrix and hard Si particles [4,5]. Despite these potential superiorities, T6 heat treatment, i.e., solid solution treatment combined with artificial ageing, must be applied to Al–Si-series alloys to realize a balanced strength-ductility combination. The former is required for dissolving and homogenizing the soluble phases, for instance, Mg_2Si and Al_2Cu phases, and for thermally improving the morphology and size of the insoluble secondary phases, such as fragmentation and spheroidization of coarse flake-like eutectic Si. The latter is conducted to promote the homogeneous precipitation of the strengthening phases from the supersaturated solid solution [6,7]. Nevertheless, in many industrial practices, the greatest challenge has been that the prerequisite solid solution treatment (at relatively high temperatures that are immediately below the eutectic-forming temperature [5]) typically gives rise to severe thermal distortion of the near-shaped thin-walled cast products, which is nearly impossible to satisfactorily amend via downstream processing. This bottleneck severely restricts their widespread application.

For resolving this dilemma, the most effective strategy is to develop a novel as-cast Al–Si-series alloy that could cater to the service conditions in view of the mechanical properties. It is reasonable to assume that this strategy will open tremendous opportunities for energy saving and the manufacture of highly complex three-dimensional components. However, limited attention and efforts have been focused on this subject

* Corresponding author. State Key Laboratory of Automotive Simulation and Control, Jilin University, PR China.
** Corresponding author. State Key Laboratory of Automotive Simulation and Control, Jilin University, PR China
E-mail addresses: qiufeng@jlu.edu.cn (F. Qiu), yanghy@just.edu.cn (H.-Y. Yang).

https://doi.org/10.1016/j.msea.2020.140247
Received 6 May 2020; Received in revised form 25 August 2020; Accepted 3 September 2020
Available online 8 September 2020

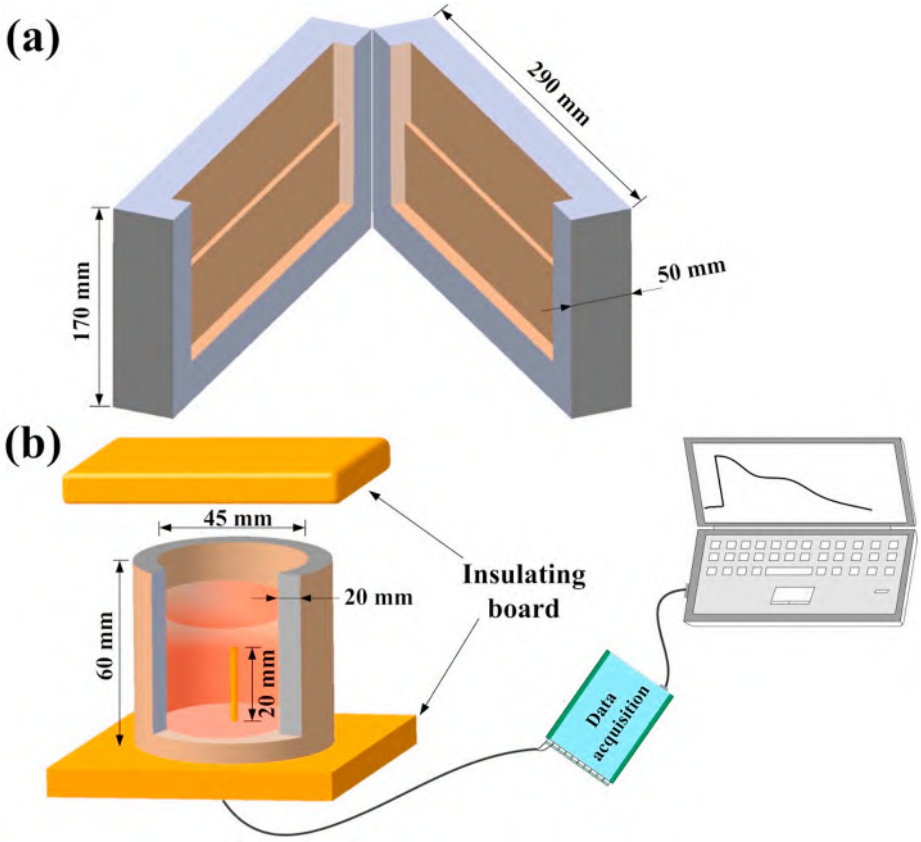

Fig. 1. Schematic illustrations of the experimental set-ups: (a) A permanent steel mold for the microstructure and mechanical property analysis and (b) a refractory brick mold for the thermal analysis.

Table 1
Chemical compositions (wt.%) of the prepared Al–Si–Mg alloys.

Alloy	Element content						
	Si	Mg	Fe	Ti	Mn	Zn	Al
Al10Si	9.8	0.01	0.11	0.02	0.010	0.010	Bal.
Al10Si0·4 Mg	9.5	0.38	0.10	0.007	0.010	0.020	Bal.
Al10Si0·8 Mg	9.7	0.79	0.09	0.01	0.002	0.008	Bal.
Al10Si1·2 Mg	9.4	1.21	0.12	0.02	0.030	0.020	Bal.
Al10Si2·0 Mg	9.8	2.02	0.11	0.02	0.006	0.009	Bal.
Al10Si3·0 Mg	9.6	2.97	0.09	0.02	0.010	0.020	Bal.

because it has been believed that the aluminum alloys in as-cast condition are always incapable of satisfying the high mechanical property requirements of structural applications. The main reason is that the uniformly dispersed nanosized precipitates under normal peak-aged conditions, which virtually constitute one of the most significant strengthening methods in metallic materials, are absent from the as-cast aluminum alloys. Additionally, under normal cooling conditions, Al–10Si-series alloys typically are featured by coarse α-Al dendrites and flaky eutectic Si with a heterogeneous distribution, which severely limits mechanical properties, especially the ductility and fracture toughness [8]. Consequently, to improve the performance of as-cast Al–10Si-series alloys, substantial efforts should be made to effectively manipulate the sizes and morphologies of the coarse α-Al dendrites, flaky eutectic Si structure and the introduction of strengthening phases. According to previous investigations of the heat-treated alloys, chemical modification via trace addition of strontium (approximately 0.01 wt%, hereafter in weight percentage) could effectively transform the needle-like eutectic Si into a fine coral-like structure [9,10]. As a result, the ductility was substantially improved, but the strength was only increased marginally. Although the addition of minor rare earth elements, such as microalloying with Sc, has been reported to simultaneously improve the strength and ductility, it is not commercially available due to its expensive cost [11,12]. Alternatively, another approach is to explore new compositional spaces that are specifically designed for as-cast service conditions by alloying in Al–10Si-series alloys [13]. Among all the alloying elements, the eutectic-forming Mg element is regarded as one of the most effective strengthening elements and could significantly improve the strength of Al–Si-series alloys after T6-tempered treatment due to the precipitation strengthening effect that is caused by Mg–Si precipitates; however, the ductility is always severely reduced as the Mg addition level is increased [14–17]. Chen et al. [16] systematically investigated the effects of Mg composition and heat treatment on the mechanical properties and found that the peak value of the ultimate tensile strength in Al–7Si–Mg alloys increased from 281 MPa to 312 MPa when the Mg addition level was increased from 0.26 to 0.58% (under solution: 540 °C × 2 h and aging: 180 °C × 12 h); meanwhile, the elongation was decreased by nearly 40%. Therefore, the addition level typically does not exceed 1.0%. J. Kang et al. [17] similarly concluded that 0.45% more addition of Mg increased the yield strength by 43 MPa in Al–7Si-0.3Mg-0.2Fe alloy and decreased the elongation by 35%. However, to the best of our knowledge, few systematic studies have been conducted on the effects of Mg solutes on the microstructures and mechanical properties of Al–10Si binary alloys under as-cast conditions.

In this study, the correlations between the solidification microstructures and the mechanical properties of the as-cast Al–10Si alloys with a wide range of eutectic-forming solute Mg additions are well established. The effects of Mg on the solidification microstructures and mechanical properties of Al–10Si alloys are systematically investigated. The underlying mechanisms that are responsible for these evolutions are also discussed. It is expected that the optimized Al–10Si-2.0 Mg alloy, in our study, will have highly promising applications in the automotive and aerospace industries worldwide due to its increased fuel efficiency,

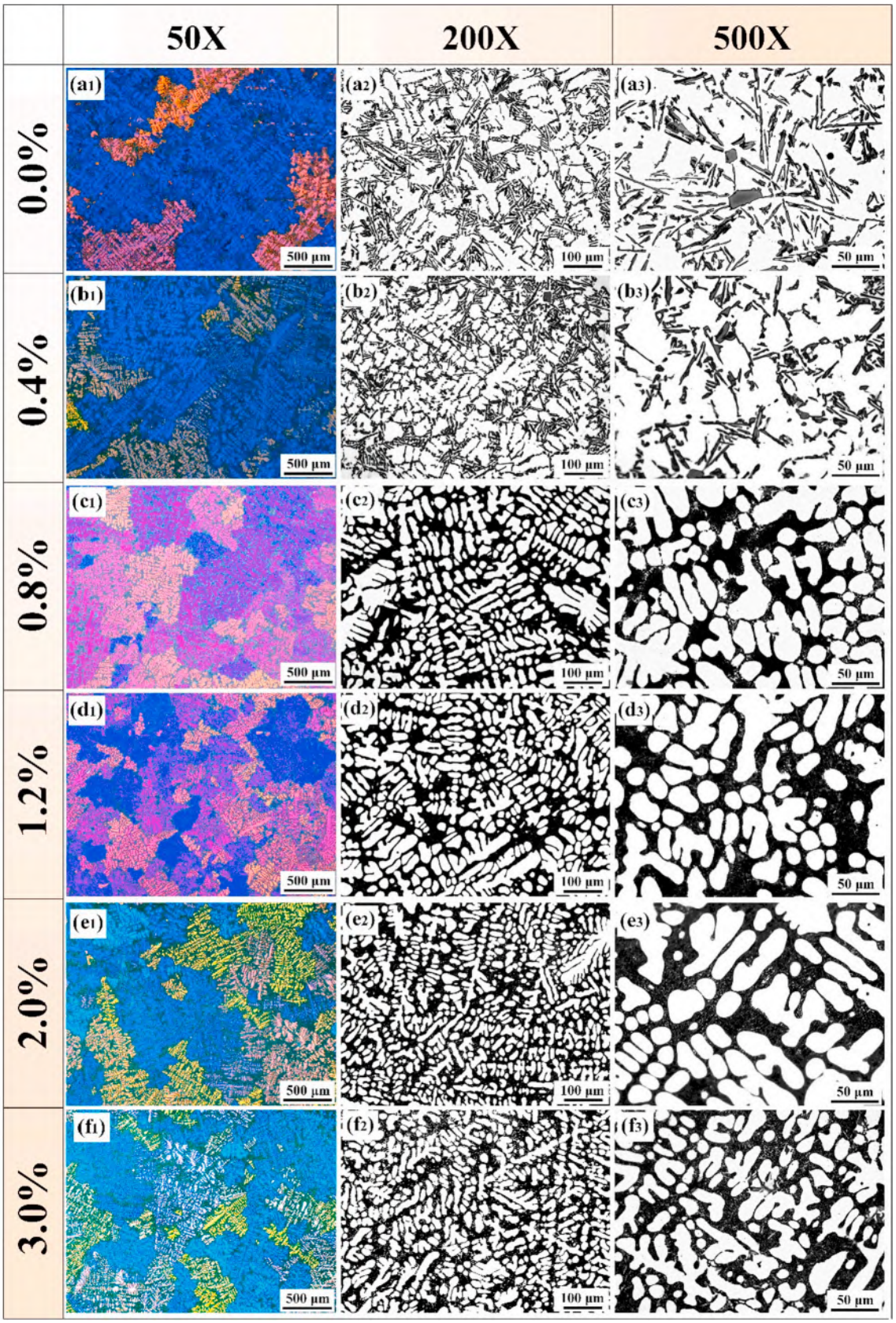

Fig. 2. Optical micrographs that show the microstructures of the as-solidified Al–10Si alloys with six addition levels of Mg element: (a_1-a_3) 0.0%; (b_1-b_3) 0.4%; (c_1-c_3) 0.8%; (d_1-d_3) 1.2%; (e_1-e_3) 2.0% and (f_1-f_3) 3.0%.

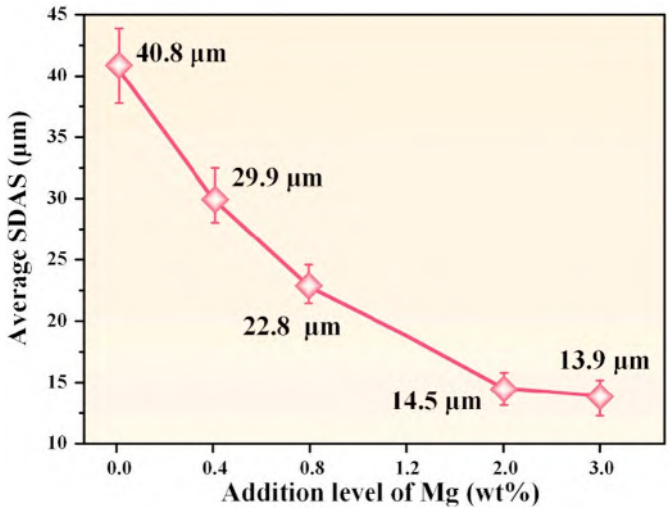

Fig. 3. Quantitative relationship between the average SDAS value of the Al–10Si-xMg alloys and the Mg addition level.

flexible structural design and fast processing.

2. Experimental materials and procedures

2.1. Material preparation

In our study, a series of Al–10Si alloys with various Mg contents were prepared from an Al–12Si master alloy, commercial pure Mg (99.9%) and pure aluminum (99.8%). First, the weighed Al–12Si master alloy and pure aluminum were melted in a graphite crucible inside an electric resistance furnace at 770 °C. After homogenization for approximately 30 min, pure Mg blocks that were wrapped in aluminum foil were carefully added and immediately pressed into the melts. After being stirred and isothermally maintained for 15 min, the melts were degassed, skimmed and poured into a permanent steel mold with inner dimensions 200 × 20 × 130 mm^3 (preheated up to 373 °C) at 750 °C, as illustrated in Fig. 1 (a). The chemical compositions of the prepared Al–Si–Mg alloys are listed in Table 1.

2.2. Thermal analysis

The temperature evolution versus the solidification time was analyzed for Al–10Si–xMg alloys without and with various Mg addition levels to determine the influence of Mg level on solidification paths of Al–10Si alloys. As illustrated in Fig. 1 (b), a cylindrical refractory brick mold of inner dimensions Φ45 × 50 mm was used to precisely characterize the solidification reaction under nearly isothermal conditions. The cooling rate was measured to be approximately 0.8 K/s. Prior to pouring, a K-type thermocouple connected with a data acquisition system was inserted into the center of the mold with the tip 20 mm away from the bottom. The pouring temperature of the molten melt was also maintained at approximately 750 °C, and the temperature data were logged at a frequency of 40 Hz during solidification. Then, according to Ref. [18], the characteristic temperatures for primary α-Al and eutectic Al–Si reaction were derived from the cooling curves (T/t) and the corresponding first derivative (dT/dt) curves, including the nucleation temperatures, minimum temperatures and growth temperatures during recalescence, which were denoted as $T_{N,\alpha\text{-}Al}$ and $T_{N,\ Al\text{–}Si}$, $T_{M,\alpha\text{-}Al}$ and $T_{M,\ Al\text{–}Si}$, $T_{G,\alpha\text{-}Al}$ and $T_{G,\ Al\text{–}Si}$, respectively.

2.3. Characterization

The metallographic specimens were mechanically ground, polished and electrochemically etched using Barker's solution. The average SDAS values (λ) of the alloys were calculated as follows [19]:

$$\lambda = \frac{L}{n} \tag{1}$$

where L is the length of the measured cells and n is the number of dendritic cells. The extraction experiment was conducted for the eutectic Si structure analysis. Firstly, small ingots were cut off from every sample and thoroughly cleaned by the ethanol. Secondly, the ingots were immersed in a beaker containing 10 vol% hydrochloric acid solution to fully dissolve the aluminum matrix. After approximately 24 h, all eutectic Si particles settled at the bottom of the breaker, then the extracted particles were collected and washed by distilled water five times to remove the residual acid solution on the particle surface. Finally, the eutectic Si particles were further washed by the ethanol, dried by drying oven, and then collected. Their length and aspect ratio were calculated as follows [20]:

$$Length = \frac{1}{m}\sum_{j=1}^{m}\left(\frac{1}{n}\sum_{i=1}^{n}(L_l)_i\right)_j \tag{2}$$

$$Aspect\ ratio = \frac{1}{m}\sum_{j=1}^{m}\left(\frac{1}{n}\sum_{i=1}^{n}\left(\frac{L_l}{L_s}\right)_i\right)_j \tag{2a}$$

where the L_l and L_s are the longest and shortest dimensions, respectively, of the eutectic Si particles and n and m are the number of the eutectic Si in one field and the number of the fields, respectively. For accurate description, over 10 spatial fields were measured using the Nano Measurer software for each specimen. The microstructure analyses were conducted on an optical microscope (OM, Olympus PMG3, Japan), a scanning electron microscopy (SEM, Tescan vega 3 XM, Czech Republic) equipped with an energy-dispersive X-ray spectroscopy (EDS) attachment, and a high-resolution transmission electron microscopy (HRTEM, JEM-2100 F, Japan). Ambient-temperature mechanical property testing (MTS 810 testing machine, USA) was conducted on the dog-bone shaped specimens with a gauge cross-section of 4.0 × 2.5 mm^2 and a gauge length of 10.0 mm after ambient temperature exposure for one week.

3. Results and discussion

3.1. SDAS of the as-cast Al–10Si-xMg alloys

Fig. 2 shows the optical microstructures of Al–10Si alloys with six addition levels of Mg: 0.0%, 0.4%, 0.8%, 1.2%, 2.0% and 3.0%. As shown in Fig. 2 (a), the typical representative microstructure of the Al–10Si binary alloy mainly consisted of coarse primary α-Al dendrites and needle-like eutectic Si in the interdendritic/intergranular eutectic regions. At around 3.0%Mg addition level, the grain size was estimated to be a reduction of 35% relative to the Mg-free Al–10Si alloy. Moreover, compared with the Mg-free Al–10Si binary alloy, the addition of Mg solute significantly suppressed the dendritic growth, and the grains grew much more dendritically. As a result, the SDAS was noticeably reduced. For reference, the SDAS values of the prepared alloys are quantitatively measured and plotted, as presented in Fig. 3. According to the statistical data, with 2.0% Mg addition, the SDAS decreased from 40.8 μm to 14.5 μm, which corresponds to a reduction of 64.5%. Further addition up to 3.0% Mg yields negligible additional refinement.

3.2. Eutectic Si structure in the as-cast Al–10Si-xMg alloys

Fig. 4 illustrates the size and morphology evolution of eutectic Si particles with the increase of the Mg addition level. As shown in Fig. 4 (a), a long acicular eutectic Si structure was exhibited by the Al–10Si binary alloy. In addition, coarse Si particles with polyhedral morphology were present due to the nonequilibrium solidification, which was similar

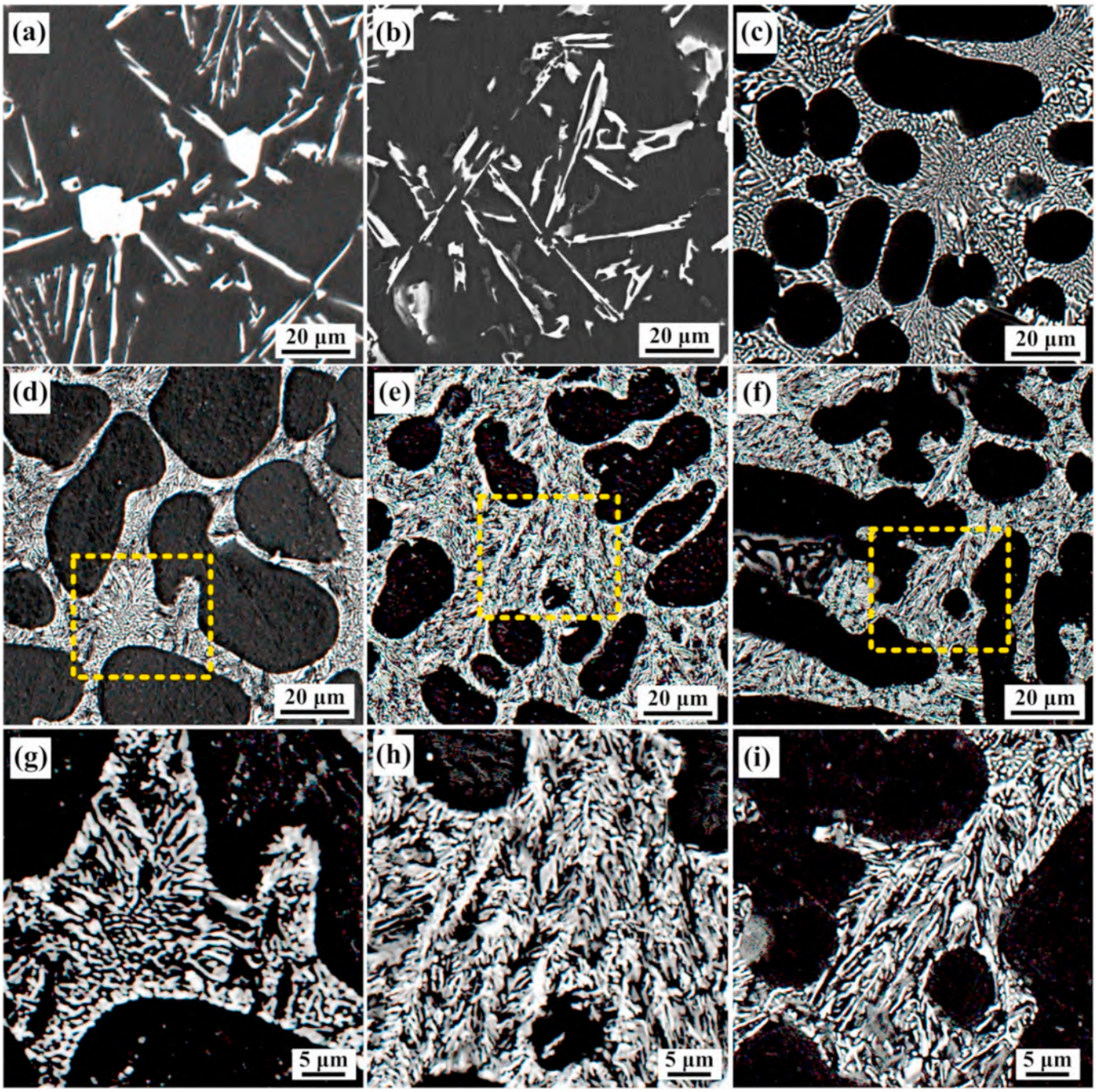

Fig. 4. Back-scattered electron (BSE) micrographs that show the eutectic Si structures of the as-cast Al–10Si alloys with six addition levels of Mg element: (a) 0.0%; (b) 0.4%; (c) 0.8%; (d) 1.2%; (e) 2.0% and (f) 3.0%. (g), (h) and (i) show magnified micrographs of (d), (e) and (f).

to the presence of primary Si particles in the hypereutectic Al–Si alloys. However, as shown in Fig. 4(b–f), the introduction of Mg substantially influenced both the size and morphology of the eutectic Si structure. Significant and continuous modification of the eutectic Si was stimulated with the increase of the Mg content. With 0.4% Mg addition, the polyhedral eutectic Si was suppressed, but the needle-like eutectic Si was still observed. When 0.8% Mg was added, a remarkable transition occurred, and the eutectic Si was significantly refined, highly branched and clustered in the interdendritic/intergranular eutectic regions. Another characteristic of this alloy is that the eutectic Si was distributed in a continuous mesh pattern. At the Mg addition level of 2.0%, a fully modified and coral-like eutectic Si structure was formed, as shown in Fig. 4(e and h). However, when the Mg level was further increased, no microstructural differences were apparent.

For further investigation of the modification efficiency change that is caused by Mg addition, the three-dimensional structures of the eutectic Si particles in the Al–10Si-xMg alloys are presented in Fig. 5. Moreover, the modification transformation of eutectic Si flakes or particles as a function of the Mg addition level was quantitatively evaluated in terms of two geometric parameters, namely, the average length and aspect ratio, as summarized in Fig. 6. As shown in Fig. 5(a), a typical large polyhedral eutectic Si particle with a size of 49.6 μm was observed in the Mg-free Al–10Si alloy. In the case of the 0.4% Mg addition level, only plate-shaped or coarser lamellar eutectic Si particles with ragged edges were observed, with an average size of 43.5 μm, as shown in Fig. 5(b). With 0.8%–1.2% Mg present, a substantial modification occurred: the

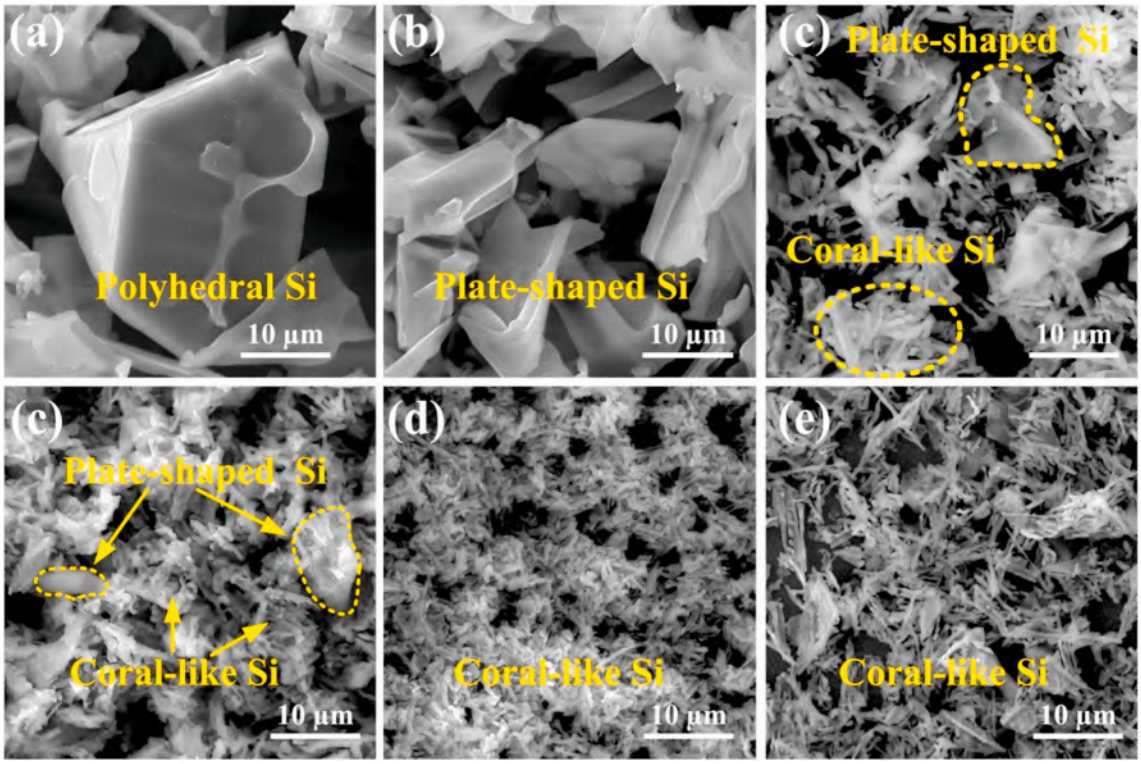

Fig. 5. SEM micrographs that show the eutectic Si structure in the as-cast Al–10Si alloys with six addition levels of Mg element: (a) 0.0%; (b) 0.4%; (c) 0.8%; (d) 1.2%; (e) 2.0% and (f) 3.0%.

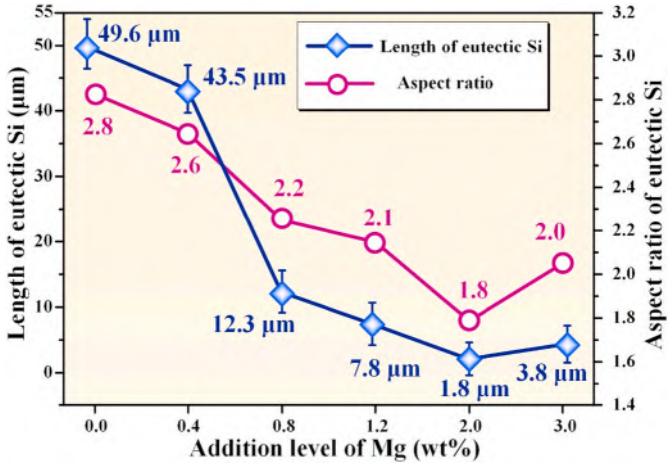

Fig. 6. Average lengths and aspect ratios of eutectic Si particles in Al–10Si alloys with various Mg addition levels.

plate-shaped structure was continually refined and branched in various directions. A mixture of branched plates and coral-like structures was observed, and the branches were progressively refined with the increase of the Mg addition. When the Al–10Si alloy was modified by 2.0% Mg, the eutectic Si particles were fully modified and exhibited a short fibrous structure that was 1.8 μm in size. By contrast, upon further addition of Mg up to 3.0%, the fibrous eutectic Si particles slightly grew in comparison with the Al–10Si alloy that contained 2.0% Mg; however, the branches remained thin. Additionally, the aspect ratio decreased nearly monotonically with the increasing Mg content and attained its minimum value at 2.0% Mg addition, as shown in Fig. 6.

3.3. Eutectic Mg_2Si in the as-cast Al–10Si-xMg alloys

The distributions of intermetallic Mg_2Si phase in the alloys with 0.4% Mg, 0.8% Mg and 2.0% Mg are presented in Fig. 7. The Mg_2Si phase was clearly distinguished from the eutectic Si by its phase contrast, which is marked with solid yellow circles in the corresponding high-magnification images and the EDS analysis. In addition, this phase was interconnected with the Al–Si eutectic phase in the interdendritic/intergranular eutectic regions. With the increase of the Mg addition level, the size of eutectic Mg_2Si phase continually decreased, and a uniform distribution was gradually realized. For 0.4% Mg, as shown in Fig. 7(a), the Mg_2Si phase, in the vicinity of the eutectic Si, exhibited a coarse and irregular rod appearance of approximately 10 μm. In contrast, in the presence of 0.8% Mg, the Mg_2Si phase was substantially refined and was approximately 3 μm in size, as identified by the EDS analysis. In the case of 2.0% Mg, the size of the Mg_2Si phase further sharply decreased and was dispersed homogeneously throughout the coral-like eutectic Si network structure, as shown in Fig. 7(c).

3.4. Mechanical properties of as-cast Al–10Si-xMg

Fig. 8(a) presents the typical engineering stress-strain curves of Al–10Si alloys as functions of the Mg addition level, and the detailed statistical data are presented in Table 2. The yield strength ($\sigma_{0.2}$), the ultimate tensile strength (σ_b) and the fracture strain (ε_f) of the binary Al–10Si alloy were 69.0 MPa, 161.6 MPa and 11.1%, respectively. With 0.4% Mg addition, $\sigma_{0.2}$ and σ_b were sustainably enhanced by 34.1% and 23.2%, and ε_f was slightly reduced due to the coarse Mg_2Si intermetallic phase. In contrast to the heat-treated Al–Si–Mg alloys, further addition of Mg simultaneously improved the strength and ductility without the common trade-off phenomenon. When the addition level was 2.0%, $\sigma_{0.2}$, σ_b and ε_f were increased to 159.4 MPa, 275.3 MPa and 14.1%, respectively, which correspond to improvements of 131.0%, 70.4% and 27.0%. Additionally, the corresponding work-hardening behavior in terms of

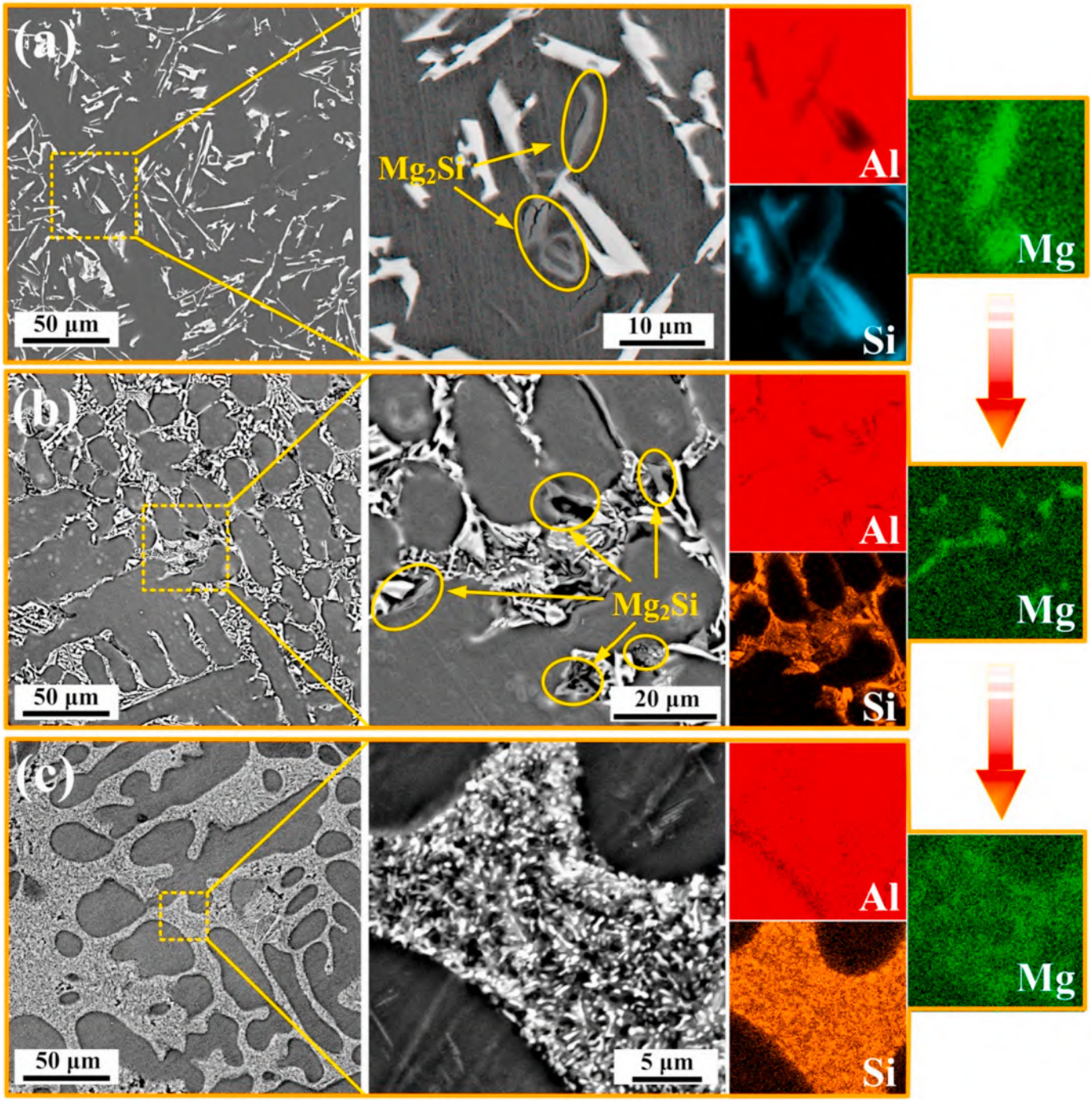

Fig. 7. BSE micrographs and EDS analysis that show the distribution of the intermetallic Mg_2Si phase in as-cast Al–10Si alloys with various addition levels of Mg element: (a) 0.4%; (b) 0.8% and (c) 2.0%.

the work-hardening rate Θ ($\Theta = d\sigma/d\varepsilon$, where ε and σ are the true stain and the true stress, respectively [21]) is presented in Fig. 8(b), which suggests the alloys with high Mg addition showed higher work-hardening rates. Nevertheless, further addition up to 3.0% adversely affected both σ_b and ε_f, which were severely reduced compared with the 2.0% level; however, they were still improved by 136.1% and 58.0%, respectively, relative to the Mg-free Al–10Si alloy. According to the SEM micrograph and the corresponding EDS results in Fig. 9, solidification defects (shrinkage cavities) were evident when 3.0% Mg was added, which strongly deteriorated the mechanical properties, especially the ductility, due to a reduction in the load-bearing area [22]. This solidification defect may be attributed to the highly increased viscosities of the melts with higher Mg contents [23]. Consistent with the results that were reported by Chen et al. [16], the shrinkage cavities exerted minimal influence on $\sigma_{0.2}$ but could significantly degrade σ_b and ε_f as they increased the stress concentration under deformation.

To comprehensively evaluate the mechanical properties, an integrated quality index, namely, *Q.I.*, was calculated in our study, which considers both the strength and the ductility and is defined as follows [17]:

$$Q.I. = UTS + klog(EI\%) \tag{3}$$

For Al–Si–Mg-series alloys, k is determined to be 150 [17]. *EI* is the

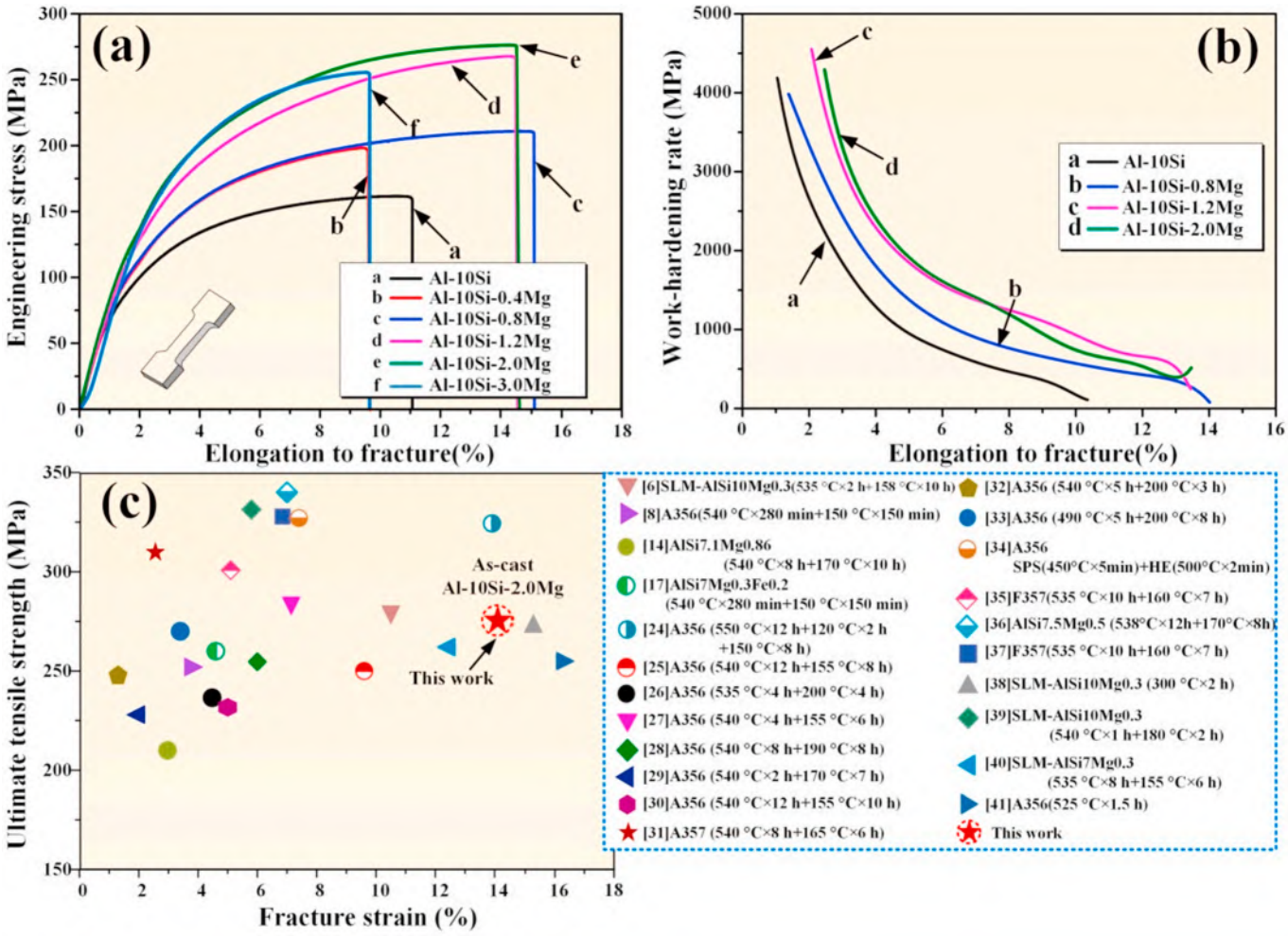

Fig. 8. (a) Engineering stress-strain curves of Al–10Si-xMg alloys with respect to various Mg addition levels. (b) Work hardening rates of the Al–10Si-xMg alloys. (c) Mechanical properties of the reported heat-treated Al–Si–Mg alloys in comparison with the properties of the alloy that we optimized in our study [6,8,14,17,24–41].

Table 2
Engineering stress-strain data statistics of the prepared Al–10*Si*-xMg alloys.

Content (%)	$\sigma_{0.2}$ (MPa)	UTS (MPa)	ε_f (%)	*EI* (%)	*Q.I.*(MPa)
0.0	69.0	161.6 ± 2.8	11.1 ± 0.7	10.0	311.6
0.4	92.5	199.1 ± 2.0	9.5 ± 0.5	8.1	335.4
0.8	95.6	211.7 ± 0.7	15.1 ± 0.6	13.7	382.2
1.2	132.2	268.7 ± 2.0	14.7 ± 0.3	12.6	433.8
2.0	159.4	275.3 ± 1.0	14.1 ± 0.7	11.7	435.5
3.0	158.0	255.1 ± 5.0	9.6 ± 1.0	7.1	382.8

elongation. The *Q.I.* values for the prepared Al–10Si-xMg alloys were calculated and are listed in Table 2. Accordingly, the optimal combination of strength and ductility was realized when 2.0% Mg was added. In addition, Fig. 8 (c) compares the mechanical properties of industrially commonly used heat-treated Al–Si–Mg alloys with the properties of the optimized alloy in our study. As observed, the Al–10Si-2.0 Mg alloy that was prepared under as-cast conditions exhibits a superior combination of strength and ductility compared to its heat-treated counterparts.

Fig. 10 shows fractographic SEM images of Al–10Si-xMg alloys under as-cast conditions. As shown in Fig. 10(a), extensive flat irregular cleavage planes and tearing ridges were presented on the surface of the fractured binary Al–10Si alloy, which implied a quasi-cleavage fracture characteristic. These large flat areas resulted from the fracture of the coarse eutectic Si particles. The microvoids were preferentially initiated at the sharp edges of the brittle lamellar eutectic Si, which were the crack initiators. After growth and coalescence, fracture occurred. These phenomena were consistent with the inferior tensile strength and ductility, as shown in Fig. 8(a). However, with 0.4% Mg addition, as shown in Fig. 10(b), the cleavage planes were substantially reduced, and dimples with uneven distribution appeared on the fracture surface. As shown in Fig. 10(d), when the Mg addition level reached 2.0%, the fracture surface was mainly covered with large quantities of well-distributed and tiny dimples, which accorded with the fully modified coral-like eutectic Si structure that is shown in Fig. 5(d). It is reasonable to assume additional stress was required for pulling the modified eutectic Si up from the eutectic α-Al. Consequently, the corresponding mechanical properties, including both the strength and ductility, were substantially enhanced. The fracture characteristic was changed to a much more ductile failure mode.

4. Discussion

4.1. Multirefinement mechanisms

The measured solidification paths with and without Mg addition and the corresponding statistical data are plotted in Fig. 11, and the detailed characteristic temperatures are summarized in Table 2. Referring to Fig. 11 (a), the addition of Mg substantially affected the solidification behaviors of the Al–10Si alloys. The three main plateaus on the derivative curves, as indicated in Fig. 11 (b), demonstrated that three transformations successively occurred after the onset of solidification,

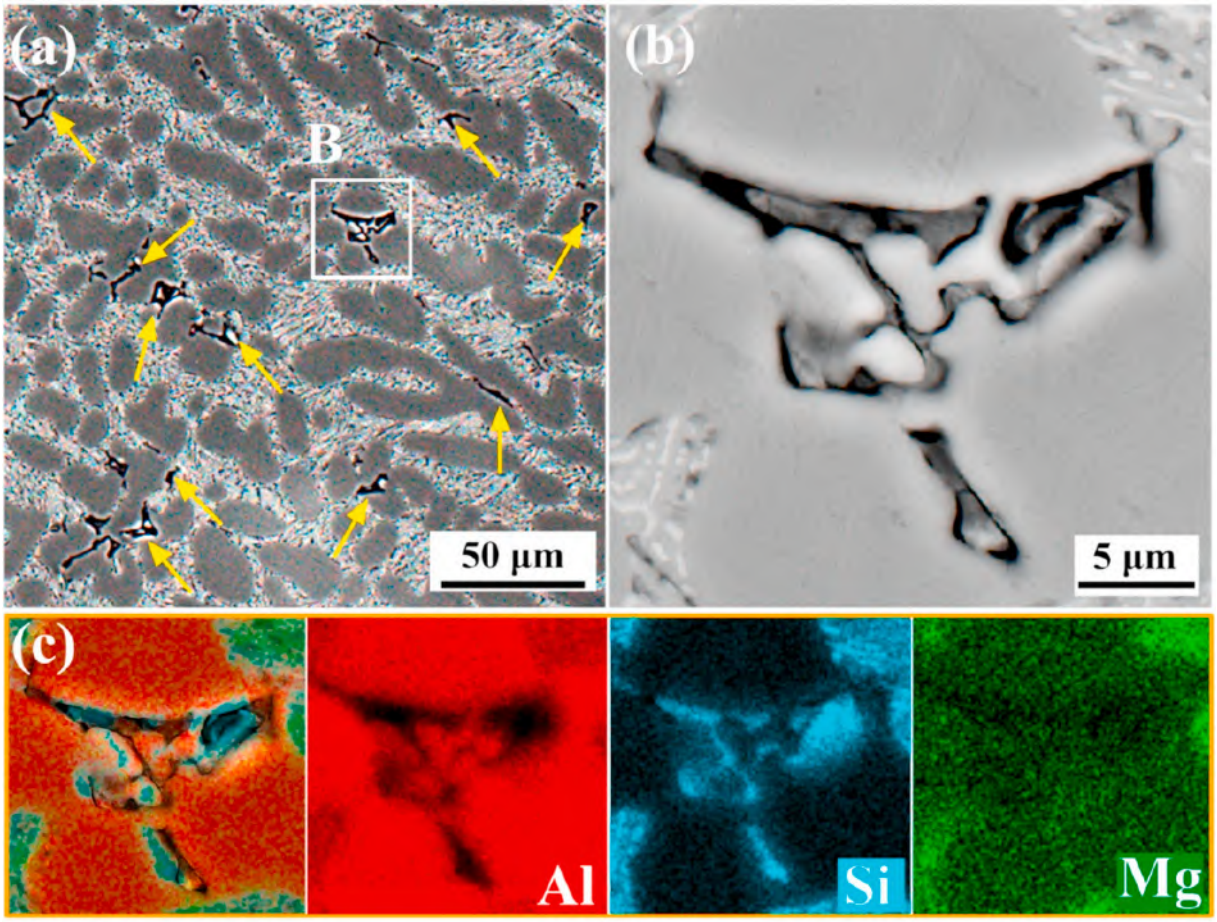

Fig. 9. (a) An SEM micrograph of the Al–10Si alloy with 3.0% Mg addition; (d) the magnification micrograph of area B in Fig. 9(a); and (c) the corresponding EDS analysis of Fig. 9(b), which shows the microstructure of the as-cast Al–10Si-3.0 Mg alloys.

namely, liquid→primary α-Al dendrites→eutectic Al–Si phase→Mg_2Si intermetallic. The addition of Mg element significantly influenced the nucleation and growth behaviors of the α-Al crystals. The cooling curves for the primary α-Al in shadowed area C in Fig. 11(a) are presented in Fig. 11(c). $T_{N,\alpha\text{-}Al}$, $T_{M,\alpha\text{-}Al}$ and $T_{G,\alpha\text{-}Al}$ decreased monotonously with the increase of the Mg addition level. For the Al–10Si alloy, $T_{N,\alpha\text{-}Al}$, $T_{M,\alpha\text{-}Al}$ and $T_{G,\alpha\text{-}Al}$ were measured to be 597.0 °C, 591.0 °C and 592.4 °C, while for the alloy with 3.0% Mg addition, these values substantially decreased to 581.4 °C, 576.2 °C and 579.0 °C, respectively.

According to previous studies [42,43], in a nucleant-free aluminum alloy, the incorporated alloying elements exert profound impacts on the dendrite size and morphology via solute partitioning. As illustrated in Fig. 12, as the partition coefficients for both Si and Mg solutes in aluminum liquid were much less than unity [42], most solutes were primarily rejected by the solidifying α-Al dendrites into the surrounding liquid upon solidification. As a result, a large amount of solutes segregated at the advancing solid/liquid (S/L) interface and a diffusion boundary layer was formed. A locally constitutionally undercooled zone was therefore developed ahead of the S/L interface, which grew over time and, in turn, triggered a wave of subsequent nucleation events on the available native potential heterogeneous nucleation sites within this region. In 1975, Maxwell and Hellawell et al. [44] proposed the growth restriction factor (GRF) Q for quantitatively evaluating the contributions of the segregating power of various solutes and contents to the grain refinement in binary alloys, which is essentially referred to the initial rate of undercooling development with respect to the fraction solid (f_s), as expressed in Eq. (4) [45]:

$$Q = \left|\frac{d\Delta T_c}{df_s}\right|_{f_{s\to 0}} = mc_0(k-1) \tag{4}$$

This solutal effect was further extended to multicomponent alloys by Desnain et al. [46], and the correlation between the solutes and the grain size (d) could be simply described by the summing contributions (Q_0) of individual solutes as follows:

$$Q_0 = \sum_{i=1}^{n} m_i c_{0i}(k_i - 1) \tag{5}$$

$$d = a + \frac{b}{Q_0} \tag{5a}$$

where m_i, c_{0i} and k_i are the slope of the liquidus, the initial concentration and the partition coefficient, respectively, of solute i and a and b could be regarded as constants. In the present study, the values of m_i and k_i for the Si and Mg solutes could be selected as −6.6 and 0.11, and −6.2 and 0.52, respectively [42]. According to Eq. (5), the Q_0 values for the alloys with Mg addition levels of 0.4%, 0.8%, 1.2%, 2.0% and 3% were calculated to be 60.2 K, 61.4 K, 62.6 K, 65.0 k and 67.9 K, respectively. According to Eq. (5a), Q_0 is inversely proportional to the grain size, and a larger Q_0 leads to a slower release of the latent heat from the growing crystals. As a result, recalescence was shifted to lower temperatures for the alloys with high Mg addition, as presented in Fig. 11(c) and Table 3. Accordingly, the grain size was reduced with the increase of the Mg addition level. However, in addition to the positive growth-restriction effect, the higher Q_0 also suppressed more potential nucleant particles close to the S/L interface due to the widened solute diffusion regions

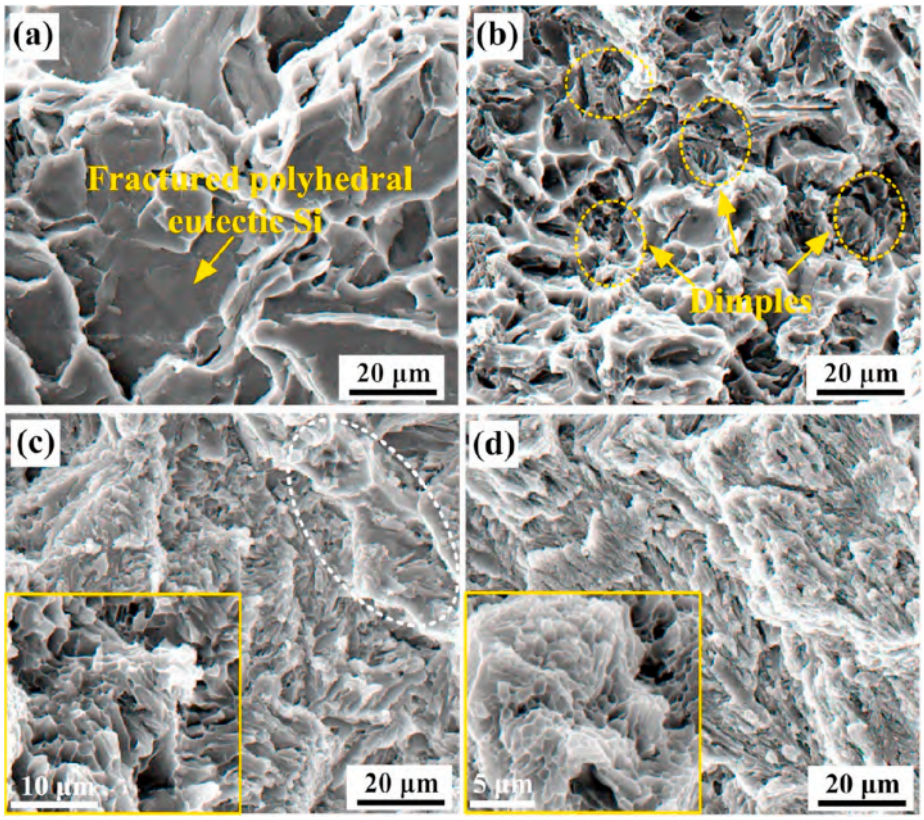

Fig. 10. SEM micrographs that show the microstructures of the as-cast Al–10Si alloys with various Mg addition levels: (a) 0.0%; (b) 0.4%; (c) 1.2% and (d) 2.0%.

[43]. Hence, the final grain size should be regarded as a compromise between the growth-restriction effect and the suppressed nucleation effects.

The secondary dendrite underwent a growth and ripening process after impinging of the dendrite tips upon each other. A mathematical model that was proposed by M. Rappaz and W.J. Boettinger et al. [47] provides a more accurate solution for the prediction of SDAS, which could be further modified as follows:

$$\lambda = 5.5(Mt)^{1/3} \tag{6}$$

$$M = \frac{-\Gamma}{\sum_{j=1}^{n}\left(Q_{0j} - Q_{fj}\right)\Big/ D_j} \ln\left[\frac{\sum_{j=1}^{n} Q_{fj}\Big/ D_j}{\sum_{j=1}^{n} Q_{0j}\Big/ D_j}\right] \tag{6a}$$

where t is the solidification time between the liquid and the solidus, Γ is the Gibbs-Thomson coefficient, Q_{0j} and Q_{fj} are the GRF for the initial and final eutectic composition at which the SDAS is determined, respectively; and D_j is the diffusion coefficient. In our study, n is determined to be 2. As shown in Fig. 11(a), t decreased with the increase of the Mg content. According to Eq. (6a), in a eutectic-containing solidification, the SDAS is largely influenced not only by the solute segregation at the beginning of solidification (Q_0), but also by that at the terminal of the primary phase solidification (Q_f), which is a more decisive factor in the restriction of SDAS coarsening, namely, the eutectic-forming Mg and residual Si solutes, which were heavily partitioned toward the end of solidification, played a more significant role in SDAS refinement.

Furthermore, when the Si concentration reached the eutectic composition, eutectic grains nucleated on the native heterogeneous substrates (most likely AlP patches or iron-rich phases [25,48]) adjacent to the tips of aluminum dendrites. According to Fig. 11(d) and Table 3, the nucleation temperature ($T_{N,\ Al–Si}$) for eutectic Si in Al–10Si alloy was 576.9 °C, which is fully consistent with that of the equilibrium transition point, namely, 577 °C for the Al-12.7Si binary alloy [48]. In contrast, the eutectic arrest temperatures changed dramatically with the addition of Mg. When the Mg content was increased, the values of $T_{N,\ Al–Si}$ for the eutectic Al–Si reaction continuously decreased. That is to say, the nucleation of the Si crystal was postponed to larger undercooling (the temperature interval between the equilibrium transition temperature and the nucleation temperature). As a result, many nucleation sites were not operated or were even stifled due to the high accumulated Mg concentration. The reduction of $T_{G,\ Al–Si}$ is a typical critical criterion that often served as an evaluation value to interpret the modification efficiency of eutectic Si growth. As proposed by M. Djurdjevic et al. [49], the Al–Si eutectic growth depression temperature, $\Delta T_{G,\ Al–Si}$, (the difference between growth temperatures in unmodified and modified alloys), is a more accurate fingerprint to be used as the on-line predictor for the modification level. The larger the magnitude of $\Delta T_{G,\ Al–Si}$, the higher the modification level. In our work, with the increasing addition level, the $T_{G,\ Al–Si}$ for alloys with various Mg additions were significantly reduced. Compared with that in the Mg-free Al–10Si alloy, the $T_{G,\ Al–Si}$ for the alloy with 2.0% Mg addition decreased by 21.7 °C, which strongly indicated that the growth of eutectic Si was substantially depressed by the Mg solutes. As observed in Fig. 13(a and b), the eutectic Si formed spheroidized branches when 2.0% Mg was added, and a high density of twinning was observed on the surface, which was consistent with the observations in Sc-modified Al–Si based alloys [35,37]. According to a previous study [50], Mg solute is a surface-active element. During Al–Si eutectic solidification, the Mg solute was further pushed and accumulated ahead of the eutectic Si and Al growth fronts at the S/L interface. Therefore, the Mg atoms were selectively absorbed in the growing eutectic Si lattice and retarded the further attachment of Si atoms onto the growing crystal, as illustrated in Fig. 13(c). As a result, the Si crystal tended to bend, curve and split radially into a coral-like structure.

Once the ternary eutectic composition was attained, the Mg_2Si

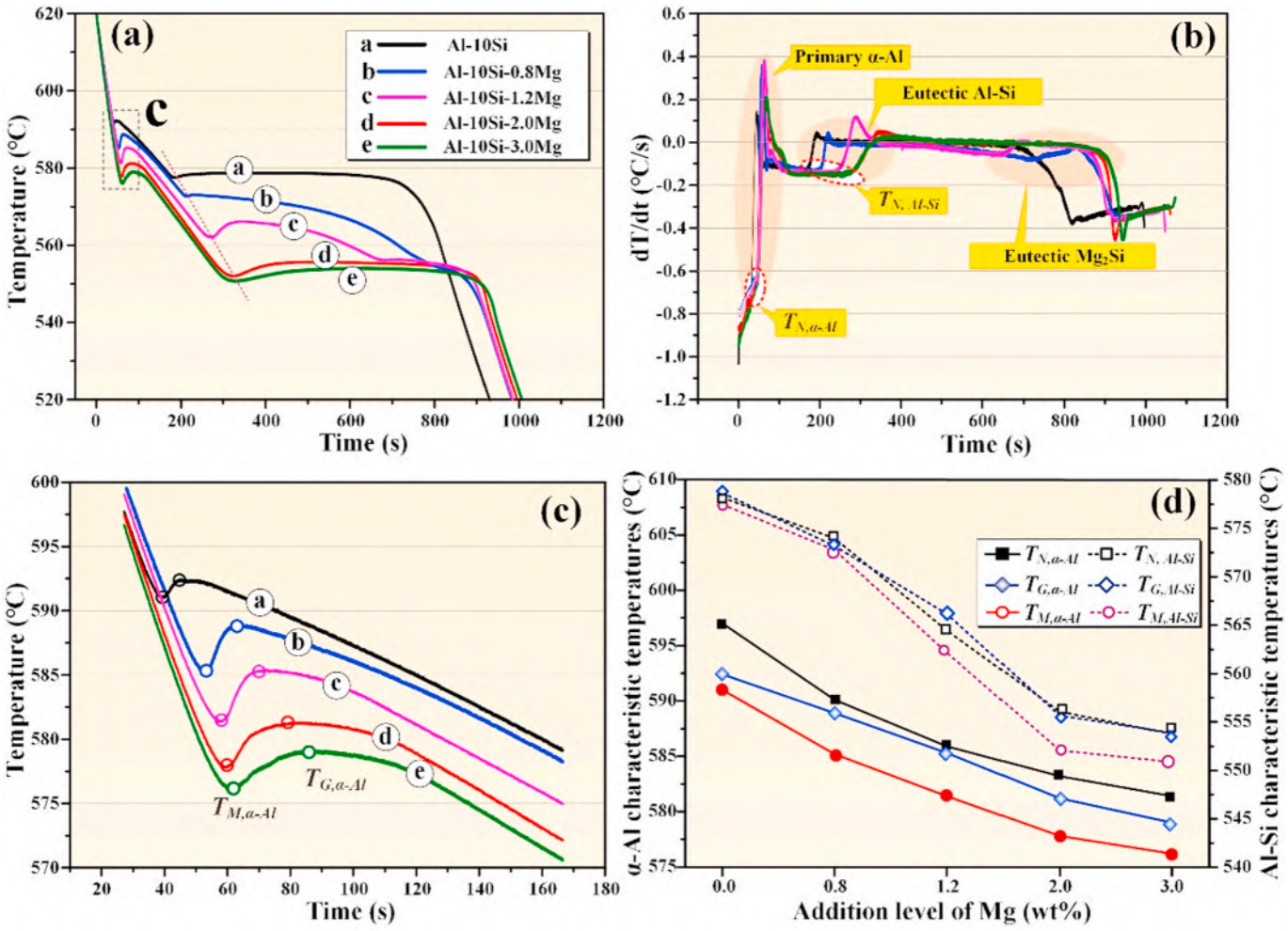

Fig. 11. Solidification histories of the Al–10Si-xMg alloys: (a) cooling curves; (b) the first derivatives (dT/dt); (c) a magnified image of shadowed region C in (a); and (d) statistical results of the characteristic temperatures.

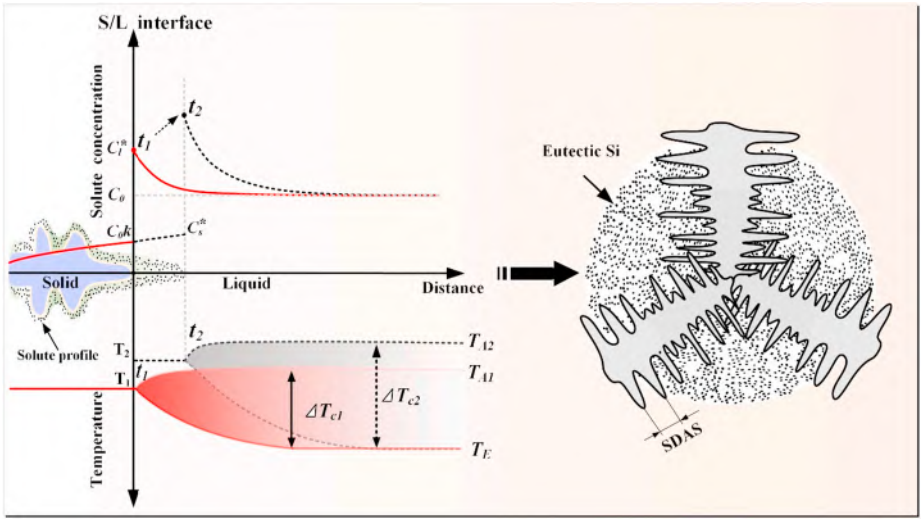

Fig. 12. Schematic illustration that shows the solute accumulation during the initial transient solidification (from t_1 to t_2) ahead of the S/L interface in the Al–10*Si*-xMg alloys. T_A is the actual temperature variation ahead of the S/L interface at a positive local thermal gradient; T_E is the equilibrium liquidus temperature; ΔT_c (T_E-T_A) is the constitutionally undercooled zone; C_l^*, C_0k, and C_0 are the solute concentrations of Mg solutes at the S/L interface in the liquid and the solid and the far-field liquid concentration, respectively.

intermetallic compound formed in the finally solidified interdendritic/intergranular eutectic regions in the vicinity of eutectic Si, which occurred at approximately 555 °C, as depicted in Fig. 11(a and b) and Fig. 13(d). Interestingly, compared with the two previous reactions, the characteristic temperatures for the Mg_2Si phase changed negligibly; nevertheless, the size of the Mg_2Si phase still progressively decreased with the increase of the Mg content, as clearly shown in Fig. 7. Thus, this refinement may be attributed to two possible mechanisms: First, the growth space of both the eutectic Si and the Mg_2Si intermetallic compound was restricted by the established dendritic skeleton network. In

Table 3
Characteristic temperatures (°C) extracted from the cooling curves of the fabricated Al–10*Si*-xMg alloys.

Alloy	Primary α-Al			Eutectic Al–Si		
	$T_{N,\alpha\text{-}Al}$	$T_{M,\alpha\text{-}Al}$	$T_{G,\alpha\text{-}Al}$	$T_{N,\ Al\text{-}Si}$	$T_{M,Al\text{-}Si}$	$T_{G,Al\text{-}Si}$
0.0	597.0	591.0	592.4	576.9	576.2	577.4
0.8	590.1	585.2	588.9	574.0	572.8	573.2
1.2	585.9	581.4	585.3	564.5	562.2	566.2
2.0	583.2	577.8	581.2	556.1	552.1	555.7
3.0	581.4	576.2	579.0	553.8	550.9	553.9

our study, the refined SDAS that was caused by the Mg addition resulted in much more tortuous dendrite boundaries. The heterogeneous distribution of the subsequently formed eutectic colonies, which included eutectic Si and Mg_2Si phases, was significantly improved. Second, the coral-like eutectic Si phases further broke up the interdendritic areas into large quantities of liquid pockets. Then, Mg and Si solutes were homogeneously dispersed among the thickets of the coral-like Al–Si network. Consequently, the available space for Mg_2Si intermetallic compound growth was severely restricted, and, hence, the Mg_2Si phase was refined as the Mg content was increased.

4.2. Strengthening and toughening mechanisms

As shown in Fig. 8, compared with the Al–10Si binary alloy, both the strength and the ductility of the as-cast Al–10Si alloys were significantly improved with high Mg addition. It is widely acknowledged that the mechanical properties depend strongly on the interaction between mobile dislocations and solidification microstructural arrangement, namely, the sizes, distributions and morphology evolutions of all the phases, which include the primary α-Al dendrite, the eutectic Si and the Mg_2Si intermetallic compound, precipitates and solidification defects in our study [16].

As substitutional atoms, Mg solutes in the interior of the α-Al matrix obstructed the dislocation movements under tensile stress. As a result, the strength was improved via solid solution strengthening, which could be qualitatively analyzed as follows [51]:

$$\Delta\sigma_{SSS} = k_{Mg}\left(C_{\alpha}^{Mg}\right)^{m} + k_{Si}\left(C_{\alpha}^{Si}\right)^{m} \tag{7}$$

where K_{Mg} and K_{Si} are the strengthening efficiencies of the Mg and Si solutes, respectively, in the solid solution (MPa wt%$^{-1}$) and C_{α}^{Mg} and C_{α}^{Si} are the concentrations of the Mg and Si solutes in the a-Al matrix (wt%). m is equal to 1 [51]. According to Ref. [23], with the increase of the Mg addition level, the amount of solution Mg solutes also increased. Hence, the yield strength progressively increased. In addition to the remaining atoms, abundant available vacancies also formed during cooling from the pouring temperature (750 °C). Individual Mg- and Si-clusters and, subsequently, Mg, Si co-clusters of several atoms naturally formed once the migrating vacancies were trapped by Mg and Si atoms during the later natural aging [52]. Under deformation, the dislocation-cluster interactions were also responsible for the significant increment of the strength in terms of (short-range) order strengthening and modulus hardening [53] or cluster strengthening [54]. It is also presumed that the number densities of these strengthening solute clusters will be substantially enhanced as the amount of Mg is increased. Additionally, the fracture, as shown in Fig. 10, was caused mainly by the cracking and propagation of brittle eutectic Si and Mg_2Si intermetallic compound in the interdendritic/intergranular eutectic regions during plastic deformation. According to the Griffith criterion [17], the correlation between the critical stress of crack propagation (σ_c) and the internal crack length (C) can be described as follows:

$$\sigma_c = \left(\frac{2E\gamma}{\pi c}\right)^{\frac{1}{2}} \tag{8}$$

where γ is the fracture surface energy and E is the Young's modulus of the eutectic Si and Mg_2Si intermetallics. In our study, compared with the coarse counterparts, the internal defects in the refined eutectic Si

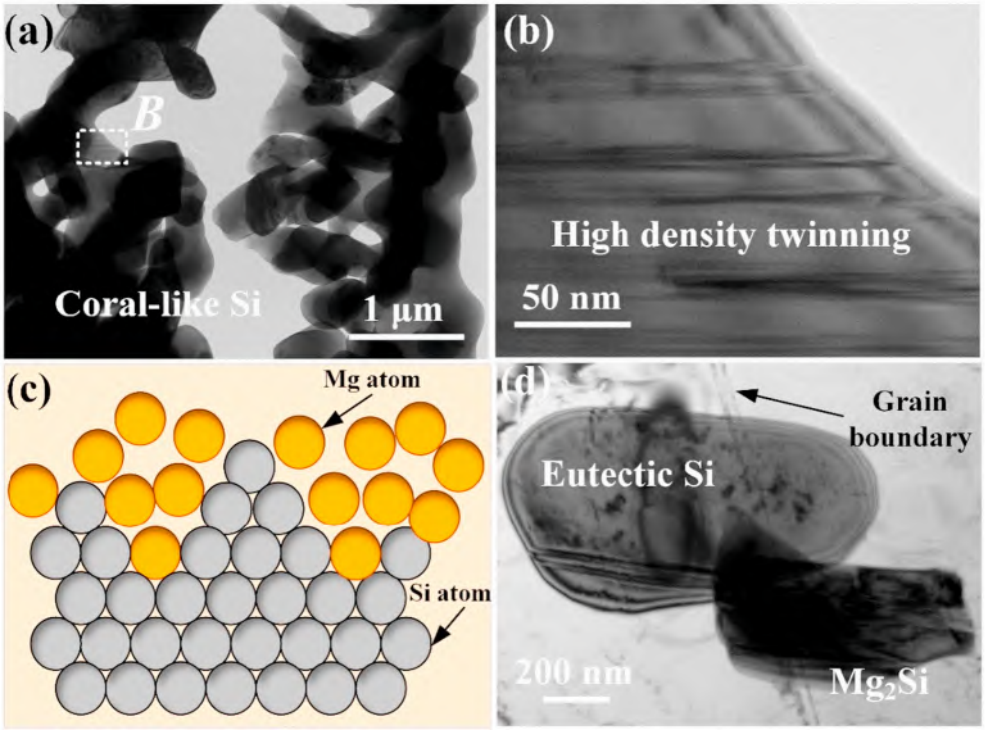

Fig. 13. (a) Coral-like eutectic Si with many spheroidized branches and (b) a magnified view of region B in (a) in the Al–10Si-2.0 Mg alloy. (c) A schematic illustration of the modification mechanism of eutectic Si via Mg addition. (d) Globular eutectic Si and Mg_2Si intermetallic phase along the grain boundary in the Al–10Si-2.0 Mg alloy.

crystals and Mg_2Si intermetallics were dramatically reduced, thereby resulting in a much lower likelihood of particle cracking, namely, larger critical fracture stress was required for crack initiation and propagation in the alloys with high Mg contents. Thus, the strength was considerably enhanced. In addition, the SDASs of the Al–10Si-xMg alloys were substantially reduced, as shown in Fig. 2. According to the grain-refinement strengthening, the resulting much more tortuous dendrite boundaries provide great potential for the improvement of strength. Additionally, the decreased SDAS tends to eliminate the formation of microporosity [55], which is also beneficial to the realization of superior mechanical properties.

Compared with the Mg-free Al–10Si alloy, crack initiation and propagation were suppressed because much more tortuous dendrite boundaries were induced by the high Mg addition level, which is directly conductive to increased ductility. Both the polyhedral and plate-shaped eutectic Si particles are detrimental to the mechanical properties, especially the ductility, because the aluminum matrix is severely split and cracks are more prone to be initiated here and propagate along the interface between the coarse eutectic Si particles and the α-Al matrix. In our study, the eutectic Si particles were transformed from the large plate-shaped structure into a rounded and fibrous morphology, which significantly relieve the stress concentrations. According to previous studies [56], the average size of the eutectic Si particles ($\overline{d_{Si}}$) and uniform elongation ($\overline{e_F}$) of the Al–Si alloys could be fitted by a lognormal relationship, which can be expressed as follows:

$$\overline{e_F} = \alpha \cdot \left(\overline{d_{Si}}\right)^{\beta} (\alpha > 0,\ \beta < 0) \tag{9}$$

where α and β are two fitting parameters. Consequently, the excellent modification of the eutectic Si particles in our study also contributed to the outstanding ductility.

5. Conclusions

In this study, a novel ternary hypoeutectic as-cast Al–10Si-2.0 Mg alloy with both high strength and high ductility was successfully optimized, which eliminated the costly and time-consuming heat treatment. The effects of ternary Mg addition in amounts that ranged from 0.0% to 3.0% on the solidification microstructures and mechanical properties of as-cast Al–10Si alloys were extensively investigated.

(1) With the increase of Mg addition, the grain size was gradually reduced. A reduction of 35% was realized at a 3.0% Mg addition level, which is mainly ascribed to the increased growth restriction factor Q_0, dependent on the initial concentrations of both Mg and Si solutes. More importantly, the secondary dendrite arm spacing decreased by 64.5%, while Q_f, which is closely related to the Mg and the residual Si contents for terminal Mg_2Si eutectic solidification, was more likely than Q_0 to be responsible for the refinement of the secondary dendrite arm spacing.
(2) With the increase of the Mg addition level, the eutectic Si particles were modified from a large plate-shape toward a rounded and fibrous morphology, which may be attributed to the suppressed nucleation and restricted growth effects that were caused by Mg addition.
(3) The increased Mg content also indirectly promoted the dramatic structural transformation of the Mg_2Si intermetallic compound from rod-like into finely dispersed particles due to the significant reduction in growing space, which was caused by the refinement of the secondary dendrite arm spacing and the eutectic Si phase.
(4) Compared with the Mg-free alloy, the mechanical properties of the as-cast Al–10Si alloy were significantly improved with increasing Mg content until the 2.0% addition level. At the 2.0% Mg addition level, the yield strength, ultimate tensile strength and fracture strain were simultaneously enhanced to 159.4 MPa, 275.3 MPa and 14.1%, respectively, which correspond to improvements of 131.0%, 70.4% and 27.0%, respectively, thereby outperforming most commonly used heat-treated Al–Si–Mg alloys. The improved mechanical properties could be attributed to the high level of Mg solutes and solute clusters as well as simultaneous refinement of the secondary dendrite arm spacing, eutectic Si and Mg_2Si intermetallic compound under a high Mg addition.

6. Data availability

The raw/processed data required to reproduce these findings would remain confidential and would not be shared at this time because the data also forms part of an ongoing study.

CRediT authorship contribution statement

Qiang Li: Writing - original draft, Methodology, Formal analysis. **Feng Qiu:** Conceptualization, Supervision, Resources, Funding acquisition, Project administration. **Bai-Xin Dong:** Supervision, Validation, Investigation. **Hong-Yu Yang:** Writing - review & editing, Supervision, Data curation. **Shi-Li Shu:** Writing - review & editing, Data curation, Formal analysis. **Min Zha:** Writing - review & editing, Supervision, Data curation, Conceptualization, Resources, Funding acquisition, Project administration.

Declaration of competing interest

The authors declare that they have no known competing financial interests or personal relationships that could have appeared to influence the work reported in this paper.

Acknowledgements

This work is supported by the National Key Research and Development Program (No. 2019YFB2006501), the National Natural Science Foundation of China (No. 51771081 and No. 51971101), the Science and Technology Development Program of Jilin Province, China (20190302004GX).

Appendix A. Supplementary data

Supplementary data related to this article can be found at https://doi.org/10.1016/j.msea.2020.140247.

References

[1] A.M.A. Mohamed, F.H. Samuel, A.M. Samuel, H.W. Doty, Influence of additives on the impact toughness of Al-10.8% Si near-eutectic cast alloys, Mater. Des. 30 (2009) 4218–4229.
[2] X.H. Gu, J.X. Zhang, X.L. Fan, N.W. Dai, Y. Xiao, L.C. Zhang, Abnormal corrosion behavior of selective laser melted AlSi10Mg alloy induced by heat treatment at 300 °C, J. Alloy. Compd 803 (2019) 314–324.
[3] P.D. Wang, H.S. Lei, X.L. Zhu, H.S. Chen, D.N. Fang, Influence of manufacturing geometric defects on the mechanical properties of AlSi10Mg alloy fabricated by selective laser melting, J. Alloys Compd. 789 (2019) 852–859.
[4] C.C. Zhang, H.H. Zhu, Z.H. Hu, L. Zhang, X.Y. Zeng, A comparative study on single-laser and multi-laser selective laser melting AlSi10Mg: defects, microstructure and mechanical properties, Mater. Sci. Eng. 746 (2019) 416–423.
[5] X.R. Liu, B. Beausir, Y.D. Zhang, W.M. Gan, H. Yuan, F.X. Yu, C. Esling, X. Zhao, L. Zuo, Heat-treatment induced defect formation in a-Al matrix in Sr-modified eutectic Al-Si alloy, J. Alloys Compd. 730 (2018) 208–218.
[6] L.F. Wang, J. Sun, X.L. Yu, Y. Shi, X.G. Zhu, L.Y. Cheng, H.H. Liang, B. Yan, L. J. Guo, Enhancement in mechanical properties of selectively laser-melted AlSi10Mg aluminum alloys by T6-like heat treatment, Mater. Sci. Eng. 734 (2018) 299–310.
[7] E. Sjölander, S. Seifeddine, The heat treatment of Al-Si-Cu-Mg casting alloys, J. Mater. Process. Technol. 210 (2010) 1249–1259.
[8] D.Y. Wu, J. Kang, Z.H. Feng, R. Su, C.H. Liu, T. Li, L.S. Wang, Utilizing a novel modifier to realize multi-refinement and optimized heat treatment of A356 alloy, J. Alloys Compd. 791 (2019) 628–640.

[9] M.D. Giovanni, J.M. Warnett, M.A. Williams, P. Srirangam, 3D imaging and quantification of porosity and intermetallic particles in strontium modified Al-Si alloys, J. Alloys Compd. 727 (2017) 353–361.
[10] M. Timpel, N. Wanderka, R. Schlesiger, T. Yamamoto, N. Lazarev, D. Isheim, G. Schmitz, S. Matsumura, J. Banhart, The role of strontium in modifying aluminium-silicon alloys, Acta Mater. 60 (2012) 3920–3928.
[11] Z. Lu, L.J. Zhang, Thermodynamic description of the quaternary Al-Si-Mg-Sc system and its application to the design of novel Sc-additional A356 alloys, Mater. Des. 116 (2017) 427–437.
[12] W.Y. Liu, W.L. Xiao, C. Xu, M.W. Liu, C.L. Ma, Synergistic effects of Gd and Zr on grain refinement and eutectic Si modification of Al-Si cast alloy, Mater. Sci. Eng. 693 (2017) 93–100.
[13] J.G.S. Macías, C. Elangeswaran, L. Zhao, B.V. Hooreweder, J. Adrien, E. Maire, J. Y. Buffière, W. Ludwig, P.J. Jacques, A. Simar, Ductilisation and fatigue life enhancement of selective laser melted AlSi10Mg by friction stir processing, Scripta Mater. 170 (2019) 124–128.
[14] M. Yıldırım, D. Özyürek, The effects of Mg amount on the microstructure and mechanical properties of Al-Si-Mg alloys, Mater. Des. 51 (2013) 767–774.
[15] Q.G. Wang, Microstructural effects on the tensile and fracture behavior of aluminum casting alloys A356/357, Metall. Mater. Trans. 34A (2003) 2887–2899.
[16] R. Chen, Q. Xu, H. Guo, Z. Xia, Q. Wu, B. Liu, Correlation of solidification microstructure refining scale, Mg composition and heat treatment conditions with mechanical properties in Al-7Si-Mg cast aluminum alloys, Mater. Sci. Eng. 685 (2017) 391–402.
[17] J. Kang, R. Su, D.Y. Wu, C.H. Liu, T. Li, L.S. Wang, B. Narayanaswamy, Synergistic effects of Ce and Mg on the microstructure and tensile properties of Al-7Si-0.3Mg-0.2Fe alloy, J. Alloys Compd. 796 (2019) 267–278.
[18] Q. Li, F. Qiu, B.X. Dong, X. Gao, S.L. Shu, H.Y. Yang, Q.C. Jiang, Processing, multiscale microstructure refinement and mechanical property enhancement of hypoeutectic Al-Si alloys via in situ bimodal-sized TiB_2 particles, Mater. Sci. Eng. 777 (2020) 139081.
[19] L. Ceschini, Alessandro Morri, Andrea Morri, A. Gamberini, S. Messieri, Correlation between ultimate tensile strength and solidification microstructure for the sand cast A357 aluminium alloy, Mater. Des. 30 (2009) 4525–4531.
[20] L.F. Li, D.Q. Li, F. Mao, J. Feng, Y.Z. Zhang, Y.L. Kang, Effect of cooling rate on eutectic Si in Al-7.0Si-0.3Mg alloys modified by La additions, J. Alloys Compd. 826 (2020) 154206.
[21] B. Chen, S.K. Moon, X. Yao, G. Bi, J. Shen, J. Umeda, K. Kondoh, Strength and strain hardening of a selective laser melted AlSi10Mg alloy, Scripta Mater. 141 (2017) 45–49.
[22] H.C. Long, J.H. Chen, C.H. Liu, D.Z. Li, Y.Y. Li, The negative effect of solution treatment on the age hardening of A356 alloy, Mater. Sci. Eng. 566 (2013) 112–118.
[23] T. Kimura, T. Nakamoto, T. Ozaki, K. Sugita, M. Mizuno, H. Araki, Microstructural formation and characterization mechanisms of selective laser melted Al-Si-Mg alloys with increasing magnesium content, Mater. Sci. Eng. 754 (2019) 786–798.
[24] M.L. Wang, D. Chen, Z. Chen, Y. Wu, F.F. Wang, N.H. Ma, H.W. Wang, Mechanical properties of in-situ TiB_2/A356 composites, Mater. Sci. Eng. 590 (2014) 246–254.
[25] F. Mao, G.Y. Yan, Z.J. Xuan, Z.Q. Cao, T.M. Wang, Effect of Eu addition on the microstructures and mechanical properties of A356 aluminum alloys, J. Alloys Compd. 650 (2015) 896–906.
[26] Z.M. Shi, Q. Wang, G. Zhao, R.Y. Zhang, Effects of erbium modification on the microstructure and mechanical properties of A356 aluminum alloys, Mater. Sci. Eng. 626 (2015) 102–107.
[27] S.M. Ma, X.M. Wang, Mechanical properties and fracture of in-situ Al_3Ti particulate reinforced A356 composites, Mater. Sci. Eng. 754 (2019) 46–56.
[28] S.L. Pramod, Ravikirana, A.K. Prasada Rao, B.S. Murty, Srinivasa R. Bakshi, Microstructure and mechanical properties of as-cast and T6 treated Sc modified A356-5TiB_2 in-situ composite, Mater. Sci. Eng. 739 (2019) 383–394.
[29] Z.W. Liu, N. Cheng, Q.L. Zheng, J.H. Wu, Q.Y. Han, Z.F. Huang, J.D. Xing, Y.F. Li, Y.M. Gao, Processing and tensile properties of A356 composites containing in situ small-sized Al_3Ti particulates, Mater. Sci. Eng. 710 (2018) 392–399.
[30] T.M. Wang, Y.P. Zheng, Z.N. Chen, Y.F. Zhao, H.J. Kang, Effects of Sr on the microstructure and mechanical properties of in situ TiB_2 reinforced A356 composite, Mater. Des. 64 (2014) 185–193.
[31] W.M. Jiang, Z.T. Fan, Y.C. Dai, C. Li, Effects of rare earth elements addition on microstructures, tensile properties and fractography of A357 alloy, Mater. Sci. Eng. 597 (2014) 237–244.
[32] M. Colombo, E. Gariboldi, A. Morri, Er addition to Al-Si-Mg-based casting alloy: effects on microstructure, room and high temperature mechanical properties, J. Alloy. Compd. 708 (2017) 1234–1244.
[33] P.T. Li, S.D. Liu, L.L. Zhang, X.F. Liu, Grain refinement of A356 alloy by Al-Ti-B-C master alloy and its effect on mechanical properties, Mater. Des. 47 (2013) 522–528.
[34] J.M. Liang, C. Kong, M.Z. Quadir, Y.F. Zheng, X. Yao, P. Munroe, D.L. Zhang, Microstructure and mechanical properties of a bulk ultrafine grained Al-7Si-0.3Mg alloy produced by thermomechanical consolidation of a nanocrystalline powder, Mater. Sci. Eng. 658 (2016) 192–202.
[35] C. Xu, W.L. Xiao, R.X. Zheng, S. Hanada, H. Yamagata, C.L. Ma, The synergic effects of Sc and Zr on the microstructure and mechanical properties of Al-Si-Mg alloy, Mater. Des. 88 (2015) 485–492.
[36] B. Li, H.W. Wang, J.C. Jie, Z.J. Wei, Effects of yttrium and heat treatment on the microstructure and tensile properties of Al-7.5Si-0.5Mg alloy, Mater. Des. 32 (2011) 1617–1622.
[37] C. Xu, W.L. Xiao, S. Hanada, H. Yamagata, C.L. Ma, The effect of scandium addition on microstructure and mechanical properties of Al-Si-Mg alloy: a multi-refinement modifier, Mater. Char. 110 (2015) 160–169.
[38] L.C. Zhuo, Z.Y. Wang, H.J. Zhang, E.H. Yin, Y.L. Wang, T. Xu, C. Li, Effect of post-process heat treatment on microstructure and properties of selective laser melted AlSi10Mg alloy, Mater. Lett. 234 (2019) 196–200.
[39] L. Girelli, M. Tocci, M. Gelfi, A. Pola, Study of heat treatment parameters for additively manufactured AlSi10Mg in comparison with corresponding cast alloy, Mater. Sci. Eng. 739 (2019) 317–328.
[40] T. Kimura, T. Nakamoto, Microstructures and mechanical properties of A356 (AlSi7Mg0.3) aluminum alloy fabricated by selective laser melting, Mater. Des. 89 (2016) 1294–1301.
[41] Z.F. Wei, Y.S. Lei, H. Yan, X.H. Xu, J.J. He, Microstructure and mechanical properties of A356 alloy with yttrium addition processed by hot extrusion, J. Rare Earths 37 (2019) 659–667.
[42] M. Easton, D.H. StJohn, Grain refinement of aluminum alloys: part I. The nucleant and solute paradigms-a review of the literature, Metall. Mater. Trans. 30 (6) (1999) 1613–1623.
[43] D. Shu, B. Sun, J. Mi, P.S. Grant, A quantitative study of solute diffusion field effects on heterogeneous nucleation and the grain size of alloys, Acta Mater. 59 (2011) 2135–2144.
[44] I. Maxwell, A. Hellawell, A simple model for grain refinement during solidification, Acta Metall. 23 (1975) 229–237.
[45] M.A. Easton, D.H. StJohn, A model of grain refinement incorporating alloy constitution and potency of heterogeneous nucleant particles, Acta Mater. 49 (2001) 1867–1878.
[46] P. Desnain, Y. Fautrelle, J.L. Meyer, J.P. Requet, F. Durand, Prediction of equiaxed grain density in multicomponent alloys, stirred electromagnetically, Acta Metall. Mater. 38 (1990) 1513–1523.
[47] M. Rappaz, W.J. Boettinger, On dendritic solidification of multicomponent alloys with unequal liquid diffusion coefficients, Acta Mater. 47 (11) (1999) 3205–3219.
[48] S.M. Liang, R. Schmid-Fetzer, Phosphorus in Al-Si cast alloys: thermodynamic prediction of the AlP and eutectic (Si) solidification sequence validated by microstructure and nucleation undercooling data, Acta Mater. 72 (2014) 41–56.
[49] M. Djurdjevic, H. Jiang, J. Sokolowski, On-line prediction of aluminum-silicon eutectic modification level using thermal analysis, Mater. Char. 46 (2001) 31–38.
[50] H.T. Li, Y. Wang, Z. Fan, Mechanisms of enhanced heterogeneous nucleation during solidification in binary Al-Mg alloys, Acta Mater. 60 (2012) 1528–1537.
[51] K.V. Yang, P. Rometsch, C.H.J. Davies, A. Huang, X.H. Wu, Effect of heat treatment on the microstructure and anisotropy in mechanical properties of A357 alloy produced by selective laser melting, Mater. Des. 154 (2018) 275–290.
[52] S. Pogatscher, H. Antrekowitsch, H. Leitner, T. Ebner, P.J. Uggowitzer, Mechanisms controlling the artificial aging of Al-Mg-Si alloys, Acta Mater. 59 (2011) 3352–3363.
[53] S. Pogatscher, H. Antrekowitsch, H. Leitner, D. Pöschmann, Z.L. Zhang, P. J. Uggowitzer, Influence of interrupted quenching on artificial aging of Al-Mg-Si alloys, Acta Mater. 60 (2012) 4496–4505.
[54] R.K.W. Marceau, A.D. Vaucorbeil, G. Sha, S.P. Ringer, W.J. Poole, Analysis of strengthening in AA6111 during the early stages of aging: atom probe tomography and yield stress modelling, Acta Mater. 61 (2013) 7285–7303.
[55] C.L. Yang, Q.L. Zhao, Z.J. Zhang, L.L. Li, W.S. Tian, R. Liu, P. Zhang, Y.J. Xu, Y. J. Li, Z.F. Zhang, Q.C. Jiang, R.O. Ritchie, Nanoparticle additions promote outstanding fracture toughness and fatigue strength in a cast Al-Cu alloy, Mater. Des. 186 (2020) 108221.
[56] C. Xu, C.L. Ma, Y.F. Sun, S. Hanada, G.X. Lu, S.K. Guan, Optimizing strength and ductility of Al-7Si-0.4Mg foundry alloy: role of Cu and Sc addition, J. Alloys Compd. 810 (2019) 151944.